Rock Mech Rock Eng (2010) 43:123–133
DOI 10.1007/s00603-009-0049-x

ORIGINAL PAPER

# Dilation and Spalling in Axially Compressed Beams Subjected to Bending

**N. Cho · C. D. Martin · D. C. Sego · J. Jeon**

Received: 9 August 2008 / Accepted: 31 March 2009 / Published online: 21 April 2009
© Springer-Verlag 2009

**Abstract** Laboratory testing of rectangular beams using a synthetic rock was used to investigate the onset of dilation and spalling. The beams are axially compressed and subjected to 4-point bending to provide non-uniform compressive stresses. The maximum tangential stress occurs at the top of the beam and rapidly decreases with distance from the top of the beam. This stress distribution was used to simulate the maximum tangential stress distribution found around circular excavations. The results showed using this beam test configuration that the onset of dilation based on beam displacement and visually observed spalling began at approximately the same stress level. Discrete element numerical analyses (particle flow code) were used to evaluate the stress path at various locations in the beams. The analyses revealed that spalling and dilation in the beams occurred well below the peak strength failure envelope determined from conventional laboratory tests. The findings suggest that the onset of dilation in laboratory tests appears to be a good indicator for assessing the stress magnitudes required to initiate spalling.

**Keywords** Beam · Rock · Spalling · Dilation · Fracture · Discrete · PFC

N. Cho (✉)
Seoyeong Engineering Co., Ltd,
14-4, Gaepo-Dong, Gangnam-Gu,
Seoul 135-240, Korea
e-mail: ncho@seoyeong.co.kr

C. D. Martin
Departments of Civil and Environmental Engineering,
University of Alberta, 3-071 NREF Building,
Edmonton, AB T6G 2W2, Canada
e-mail: derek.martin@ualberta.ca

D. C. Sego
Departments of Civil and Environmental Engineering,
University of Alberta, 3-074 NREF Building,
Edmonton, AB T6G 2W2, Canada
e-mail: dave.sego@ualberta.ca

J. Jeon
Department of Construction Information Engineering,
Induk Institute of Technology, 14 Choansan-gil,
Nowon-gu, Seoul 139-749, Korea
e-mail: jsjeon@induk.ac.kr

## 1 Introduction

The pioneering work by Fairhurst and Cook (1966) showed that axial splitting, i.e., slabbing (synonymously referred to as spalling), is a common phenomena observed in both unconfined laboratory testing and around overstressed underground openings (Fig. 1). As noted by Fairhurst and Cook (1966) spalling in laboratory compression tests is promoted by the insertion of "friction reducers" between the platens and the samples. However, around underground openings these friction reducers are absent; yet spalling is commonly observed when the tangential stresses on the boundary of the excavation exceed the rock mass spalling strength. In situ experiments in crystalline rock at AECL's Underground Research Laboratory and SKB's Äspö Hard Rock Laboratory have shown that the in situ rock mass spalling strength was approximately 56% of the laboratory uniaxial compressive strength in both massive unfractured granite and heterogeneous fractured diorite (Martin 1997; Andersson 2007).

The work by Brace et al. (1966), Tapponnier and Brace (1976), Lajtai (1974) and Martin and Chandler (1994) showed using laboratory compression tests, that many rocks start to dilate when axially aligned cracks initiate at stress levels that ranged between 40 and 60% of the peak

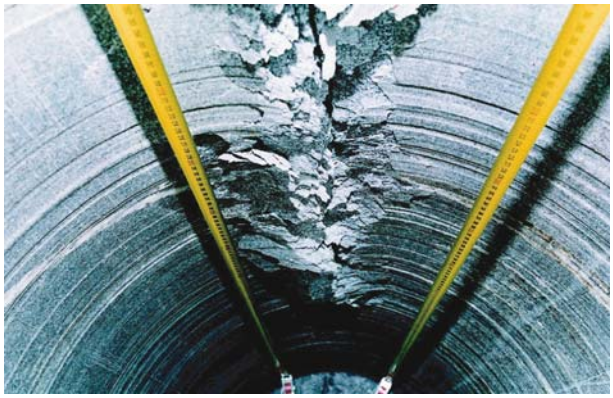

**Fig. 1** Spalling observed in a 600-mm diameter borehole in massive unfractured granite. Note the extensive dilation associated with the spalling process

laboratory uniaxial compressive strength and Cho et al. (2007) provide a discussion on dilational processes in brittle rocks. Martin (1997) and more recently Andersson (2007) showed the in situ spalling strength is in close agreement with the onset of dilation measured in laboratory uniaxial compression tests. The in situ strength reduction reported by Andersson (2007) and Martin (1997) was observed around circular openings, however, similar strength reductions have been reported for other shaped openings in other rock types (Martin et al. 1999). There is little doubt that the in situ spalling rock mass strength is considerably less than the measured laboratory uniaxial compressive strength for many rocks. However, it is not clear if the agreement between the in situ rock mass spalling strength and the onset of dilation in laboratory compression tests is fortuitous, as spalling is not observed at the onset of dilation in laboratory compression tests. To shed light on this issue laboratory tests are needed that capture dilation and spalling and its characteristics.

Hoek (1965) experimentally explored fracturing around a circular opening using thin plates containing a 25-mm diameter hole and subjected to uniaxial and biaxial loading conditions. Since then other experimental approaches to simulate fracturing around boreholes or tunnel excavation have been explored, e.g., Gay (1973), Santarelli and Brown (1989), Ewy and Cook (1990), Haimson and Song (1993), Lee and Haimson (1993), Dzik (1996), Sellers and Klerck (2000). Many of these laboratory tests have been restricted to small scale circular holes, ranging in diameter from 6 to 110 mm. However, as noted by Martin et al. (1994) there is a significant strength scale-effect observed when the diameter of these holes is <75 mm.

In this paper, laboratory testing of rectangular beams is used to investigate the onset of dilation and spalling. Beams loaded axially in compression combined with bending provide a stress path that results in non-uniform stresses similar to those expected around an underground

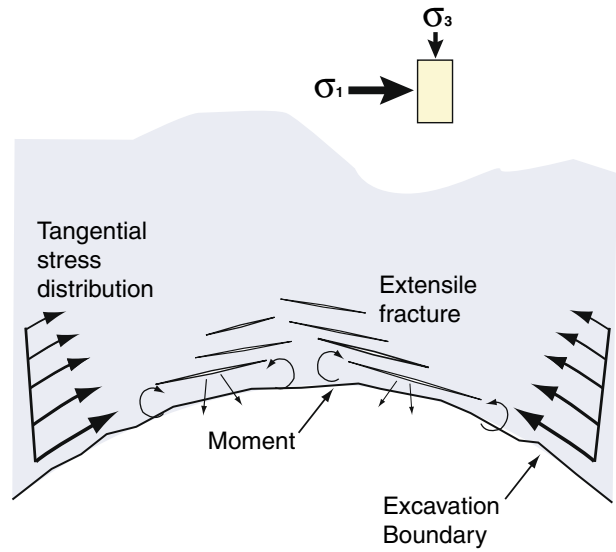


**Fig. 2** Illustration of the non-uniformly distributed tangential stress near the boundary underground

excavation. In addition, these tests remove the strength scale dependency found for circular holes. Simulation of the tests was conducted using a discrete element method (DEM) to investigate the progressive nature of dilation and spalling process as the loads on the beam are applied.

## 2 Experimental Setup

As schematically illustrated in Fig. 2, the overstressed zone around an underground opening is normally subjected to both non-uniformly distributed compressive (tangential) stresses and potentially moment loading induced by formation of extension fractures parallel to the direction of tangential loading. Generating such stress conditions requires boundary conditions that cannot be obtained using conventional laboratory compression tests.

Pre-stressed concrete beams are structural elements that are frequently used to resist tension when subjected to bending. An axially stressed beam when subjected to bending produces non-uniformly distributed compressive stresses as illustrated in Fig. 3. In conventional beam bending tests such as 3-point or 4-point bending, compression occurs at the upper section of the beam while tension occurs at the bottom. By superimposing an axial stress to the bending stress the entire beam can be kept in compression (Fig. 3). To ensure reasonably uniform testing specimens a synthetic weak brittle rock was used to create the beams. The detailed test scheme and characteristics of synthetic weak rock used in this study are presented in the next section.

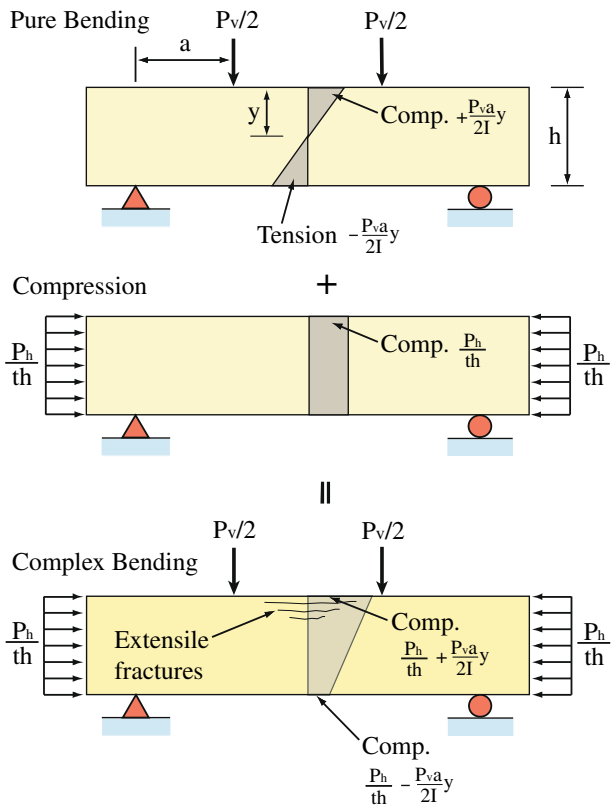


**Fig. 3** Illustration of the combined boundary loading conditions that were used to generate the non-uniform compressive stress conditions

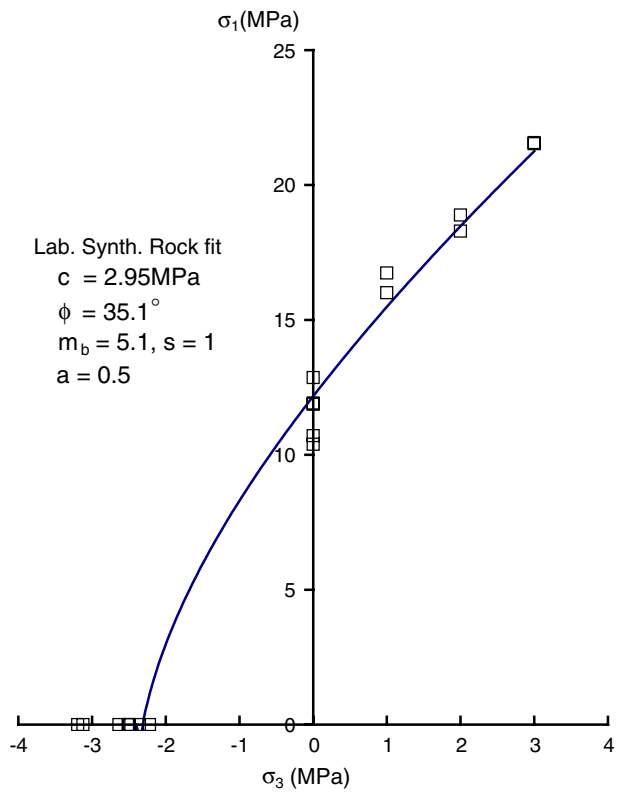


**Fig. 4** Failure envelope of the synthetic rock. The strength parameters were estimated using RocLab ver. 1.0, RocScience Inc. (2002b)

**Table 1** Material properties of Sulfaset synthetic rock

| $\sigma_c$ (MPa) | $\sigma_t$ (MPa) | $E$ (GPa) | c (MPa) | $\phi$ (deg) | $s$ | $m_b$ |
|---|---|---|---|---|---|---|
| 11.6 ± 1.0 | 2.6 ± 0.3 | 2.5 ± 0.5 | 2.95 | 35.1 | 1 | 5.07 |

$\sigma_c$ uniaxial compressive strength, $\sigma_t$ Brazilian tensile strength, $E$ Young's modulus, $c$ cohesion, $\phi$ friction angle, $s$, $m_b$ H–B material constants, ± standard deviation

## 2.1 Synthetic Rock

The synthetic weak rock used in this study was created from "sulfaset" which is generally used for setting anchor bolts. This synthetic rock has brittle characteristics but a lower compressive strength that reaches approximately 80% of its maximum strength within a few hours after moulding. The strength and stiffness of the synthetic rock is highly dependent on its initial moisture content at mixing, and for the tests reported here the initial moisture content was fixed at 50% and cured for 3 days in a constant temperature and moisture room. To induce random heterogeneity in the sample, 10% concrete sand by mass was added to all the samples. This methodology produced consistent and reproducible results (Cho et al. 2007).

Uniaxial compressive strength and tensile strength were measured from conventional uniaxial compression (55 mm × 110 mm cylinder sample) and Brazilian test. Shear strength parameters were obtained from triaxial compression testing using a Hoek cell. The measured properties are given in Table 1. Though sand is added for material heterogeneity, relatively homogeneous properties were obtained. Figure 4 shows the failure envelope for the synthetic rock and the fitted parameters for the non-linear Hoek–Brown failure envelope.

## 2.2 Axially Compressed Beam Bending System

The test beams were 88.9 mm in height, 114.3 mm in thickness and 406.4 mm in length. To provide uniform curing condition the specimens were moulded in a specially devised thick walled steel mould (10 mm thick). Tightly bolted plates covered all sample faces until the sample set (i.e., about 20 min). This allowed the sample to set without being exposed to air. The mould was then removed and cured in similar conditions as the sample used for uniaxial and triaxial testing. For the verification of beam strength, cores were taken from the moulded beam and the uniaxial strength measured was compared with that from samples cast for strength tests. Figure 5 shows the axial stress versus axial strain for a cored sample compared with the cylindrical cast sample. No significant difference

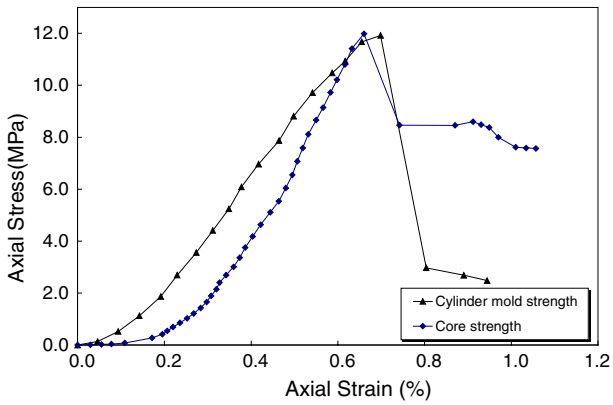


**Fig. 5** Verification of the beam strength from the core strength compared with cylinder mould strength in uniaxial compressive test

in peak strength was observed, however, the cored sample showed slightly different stress–strain response during the initial loading, possibly related to sample damage during the coring procedure.

Hydraulic rams were used for the application of axial load and bending load. As the tensile stress in the bottom region of the sample needed to be suppressed, a load ratio (i.e., bending force to axial force) of 1:3 was required to keep the sample in compression. This ratio was maintained during the test by choosing appropriate diameters for the hydraulic rams. The load controls were activated by controlling the pressure via a syringe pump. The pump pressure rate was kept constant during the test at 50 kPa/min which was slow enough to visually observe the specimen during loading. The applied pressure was recorded to the computer data logger via a transducer in 10 s capture intervals.

The axial load frame consisted of 25 mm steel plate connected with six 30-mm diameter steel rods. The frame supporting the vertical ram was provided by 10-mm thick U-sections beam. To minimize the bending moment and eccentricity of the axial load ball bearings were installed between all loading plates. For the initial seating, a pump pressure of 70 kPa that corresponds to 0.03 MPa stress at the top fibre in the beam was applied. The specimen was then loaded until failure using this system. In a circular excavation the tangential stresses are naturally concentrated due to the curvature of the openings. To concentrate the stresses at the centre of the beam a 5-mm deep 1-mm wide notch was installed at the top centre of the beam specimen using a saw. This notch is analogous to observations reported by Martin et al. (1997) where the onset of spalling around a circular test tunnel was always associated with a notch tip. Several tests were carried out with and without the notch and those tests with the notch appeared to provide the most uniform stress concentrations and best visual

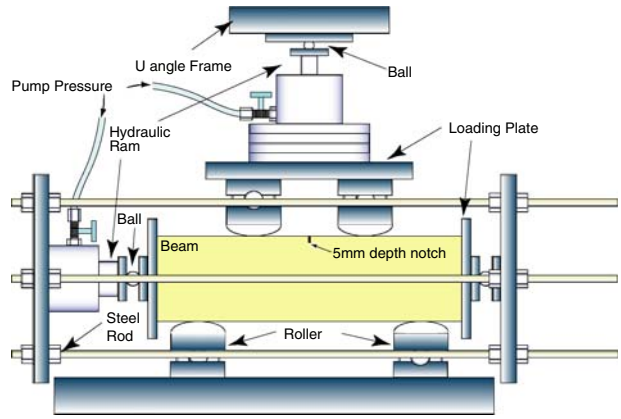


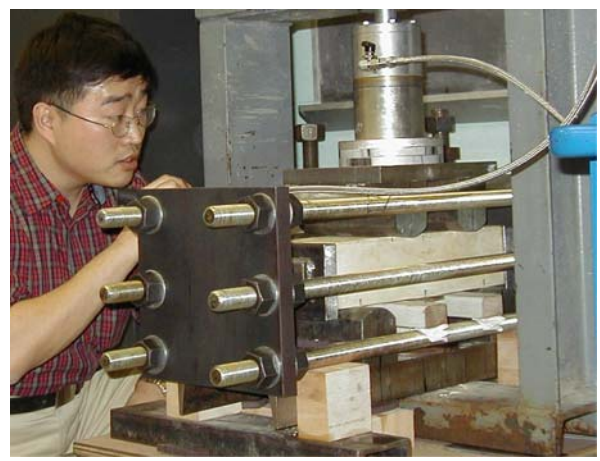

**Fig. 6** Experimental setup to simulate spalling using an axially compressed beam subjected to bending

observations. The laboratory test setup illustrated above is shown in Fig. 6.

## 3 Test Results

Stress applied at the top centre of the beam was calculated by combining axial stress and the well-known beam flexure formula (Hibbeler 1997):

$$\sigma_f = k\left(\frac{P_a}{A} \pm \frac{M}{I}y\right) \tag{3.1}$$

where $\sigma_f$ compressive stress, $P_a$ axial force, $A$ cross section area of beam, $M$ bending moment, $I$ moment of inertia, $y$ centroid of the cross section, $k$ stress concentration factor.

The stress concentration factor $k$ depends on the curvature of the notch tip and specimen dimension (Lipson and Juvinall 1963) thus it is difficult to estimate analytically. Figure 7a and b shows the distribution of the elastic stress concentration factor estimated using a two-dimensional finite element code Phase2D (RocScience Inc. 2002a). Based on the numerical results shown in Fig. 7a and b, the stress concentration factor $k$ is 3.3.

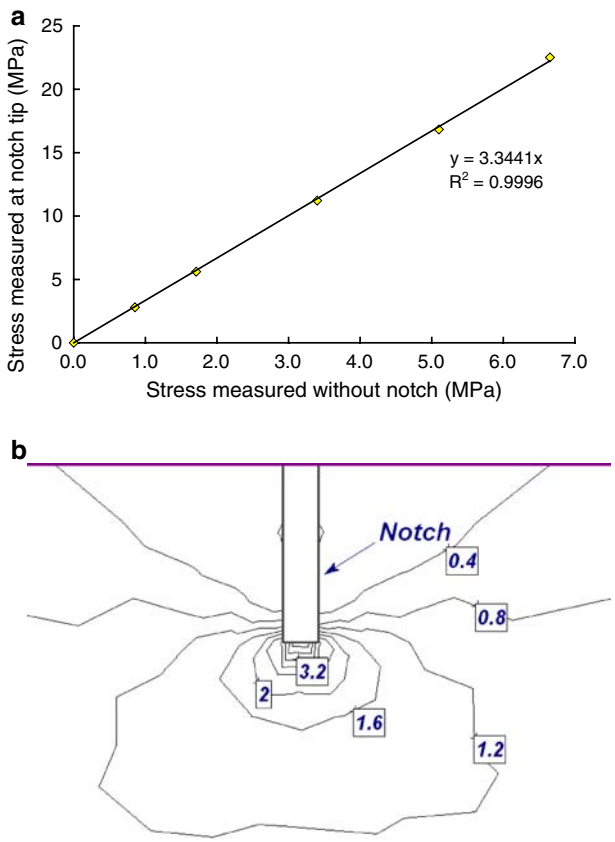


**Fig. 7** **a** Stress concentration factor (*SCF*) obtained from the elastic two-dimensional finite element code, Phase2. Note that the *horizontal axis* is the stresses calculated from Eq. 3.1 and the *slope* indicates the SCF. **b** SCF distribution near the notch tip

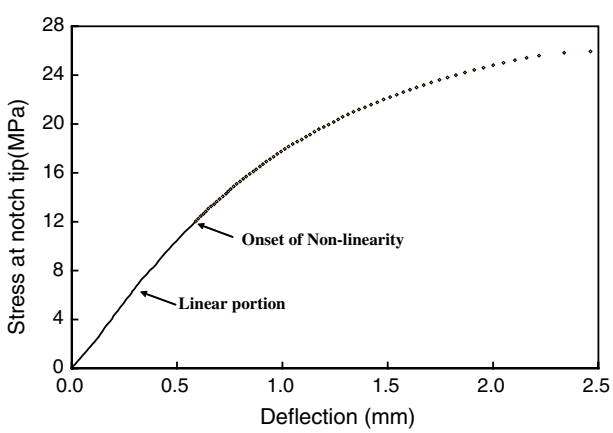


**Fig. 8** Notch tip stress calculated using the estimated stress concentration factor and the corresponding beam displacement measured at the centre of the beam. The *non-linear* portion of *graph* indicates the occurrence of localized yielding in the specimen

Figure 8 shows the relationship for the displacements measured at the centre of the beam and the stresses near the notch tip calculated using Eq. 3.1 and the estimated $k$ value. As the $k$ value in Fig. 7 was estimated using elastic analysis, it is only applicable for the elastic response and the actual stresses at the notch once localized yielding initiates is unknown. However, from Fig. 8 the linear portion of the stress–displacement plot appears to end at a stress of approximately 12 MPa, which is similar to the uniaxial compressive strength of the synthetic rock shown in Table 1. Whether this is fortuitous is not known, as it should be noted that this represents the maximum stress calculated at the notch tip and not the average stress in the region of the notch.

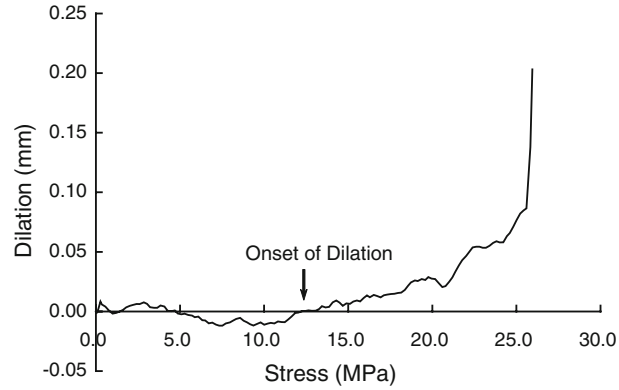


**Fig. 9** Dilation as a function of calculated stress at the notch tip. Dilation is defined as the positive difference between the displacements measured at the *top* and *bottom* of the beam

As noted by Andersson (2007) one of the notable characteristics of spalling is the significant amount of dilation associated with the spalling process. Displacements were measured at the top and bottom of each beam using LVDT's. Since the displacement at the top and bottom of the specimen should be the same if the specimen behaviour is elastic and homogeneous, a difference between top and bottom displacement could indicate dilation associated with the non-elastic fracturing/yielding in the beam. Figure 9 shows the dilation measured in a typical beam specimen. The dilation appears to initiate at approximately 12.5 MPa which is also similar to the stress level where the non-linear response commences in Fig. 8. Visual observations at the time of testing indicated that small cracks appeared near the notch tip at approximately these stress magnitudes. The test results indicate that the initiation of the non-linear portion of the stress–displacement plot corresponds approximately to the onset of visible and audible fracturing in the specimen. After fracture initiation, non-linearity becomes significant. Figure 10a and b shows the ruptured specimen shape from this test with spalling slabs similar to those shown in Fig. 1. For pure bending, i.e., no axial compression, spalling is not observed (see Fig. 11).

From the test results it was concluded that the tests can adequately simulate spalling and that the onset of spalling

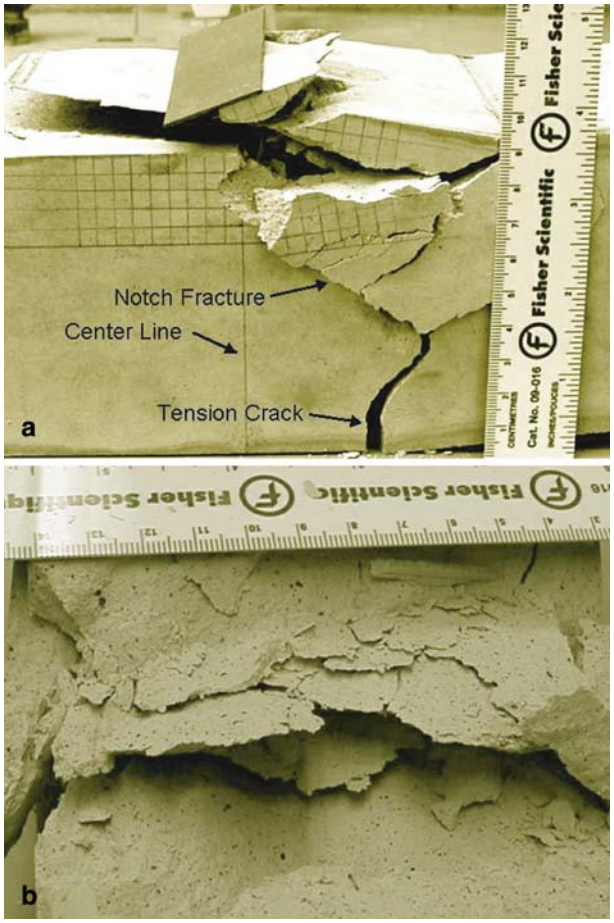


**Fig. 10** Final ruptured shape of beam specimen and the spalling observed at the *top centre*. Note the similarity to the spalling observed in Fig. 1. **a** Beam after complete failure, **b** spalling observed at the *top* of the beam after rupture

**Fig. 11** Tensile fracture observed in 4-point bending system. The tensile strength measured from this test was 1.5 MPa which is approximately 60% of the tensile strength measured in Brazilian test and shown in Table 1

is associated with the onset of dilation. In the next section, the DEM is used to simulate the beam tests described above.

## 4 Bonded Particle Analogue

### 4.1 Discrete Element Modelling

The particle flow code (PFC) is a discrete element code that represents a solid as an assemblage of circular disks connected with cohesive and frictional bonds. The DEM is used to model the forces and motions of particles within this assembly. This method is similar to that used in explicit finite difference analysis and allows crack formation and its propagation through the system (Potyondy and Cundall 2004).

In this model, the particles can move independently from one another and interact only at their contacts. They are assumed to be rigid but they overlap at the contacts under compression. Thus, particles themselves do not deform but have rigid body motion. The particles can be bonded together by specifying the shear and tensile bond strength at each contact point. The values assigned to these strengths influence the macro strength of the sample and the nature of cracking and failure that occurs under load. Friction is activated by specifying a coefficient of friction, and is mobilized while particles are in contact. Tensile cracks occur as the applied normal force on each contact exceeds the specified normal bond strength. Shear cracks are generated as the applied shear force either by rotation or shear of particles exceeds the specified shear bond strength. The tensile strength at the contact immediately becomes zero after bond breakage while the shear strength mobilized depends on specified coefficient of friction and induced normal contact force. After a bond breaks, the stress is redistributed and this may then cause adjacent additional bonds to break. The microscopic behaviour in PFC is governed by the basic micro parameters used to describe the contact stiffness, bond stiffness, bond strength and contact friction (Potyondy and Cundall 2004).

### 4.2 Micro Parameters for Synthetic Rock

Although PFC has simple contact logic, it is not easy to choose appropriate micro properties so that the behaviour of the PFC model resembles that of the physical material. The application of PFC relies on obtaining macro-scale material behaviour from the microscale interactions. While the micro properties of the real physical material are very important they are seldom known. To determine these parameters one must compare the relevant behaviour of the intended physical material with synthetic material

**Table 2** Micro parameters used to represent the Sulfaset synthetic rock

| | | | |
|---|---|---|---|
| $R_{min}$ | 0.25 mm | $E_c$ | 1.4 GPa |
| $R_{max}/R_{min}$ | 1.5 | $k_n/k_s$ | 2.5 |
| $\overline{\lambda}$ | 1.0 | $\overline{E}_c$ | 1.4 GPa |
| $\mu$ | 0.75 | $\overline{k_n}/\overline{k_s}$ | 2.5 |
| $\overline{\sigma_n}$ | 6.8 ± 1.7 MPa | *clp_rad* | 0.37 ± 0.2 mm |
| $\overline{\sigma_s}/\overline{\sigma_n}$ | 1.0 | Unit_weight | 1,830 kg/m$^3$ |

$R_{min}$ minimum particle radius, $R_{max}/R_{min}$ particle radius ratio, $\overline{\lambda}$ bond radius ratio, $\mu$ coefficient of friction, $\overline{\sigma_c}$ normal bond strength, $\overline{\sigma_s}/\overline{\sigma_n}$ bond strength ratio (shear to normal), $E_c$ contact Young's modulus, $\overline{E}_c$ bond Young's modulus, $k_n/k_s$ contact stiffness ratio, $\overline{k_n}/\overline{k_s}$ bond stiffness ratio, *clp_rad* clump radius

**Table 3** Macro properties obtained from the sample calibration

| $\sigma_c$ (MPa) | $\sigma_t$ (MPa) | $E$ (GPa) | $c$ (MPa) | $\phi$ (MPa) | $s$ | $m_b$ |
|---|---|---|---|---|---|---|
| 12.27 | 2.24 | 2.51 | 2.9 | 36.1 | 1 | 5.48 |

behaviour in PFC by choosing parameters by trial and error (Itasca Consulting Group 2004).

Cho et al. (2007) calibrated the micro parameters in PFC on the synthetic rock used in this study by performing biaxial and Brazilian test simulations. They used a clumping technique to create irregular non-spherical particle shapes. Cho et al. (2007) showed that this clumping technique removed some of known limitations in modelling brittle rock with PFC, e.g., unrealistic tensile strength and low frictional strength envelope. As the same synthetic rock was used in the bending test simulation, the identical micro properties given in Cho et al. (2007) were used in this study. The calibrated PFC micro parameters of synthetic rock are tabulated in Table 2 and the macro properties obtained from the calibrated results are given in Table 3.

### 4.3 Modelling Axially Compressed Bending Test

Axially compressed bending tests for the synthetic rock were numerically simulated using PFC2D by mimicking the laboratory configuration. Figure 12 illustrates the axially compressed bending model scheme used in the PFC model. It is desirable that a PFC model has the identical dimensions as the laboratory beam specimen. However, this would requires more than 100,000 balls to be generated with the currently calibrated PFC model. Increasing the number of particles for composing the sample assembly not only requires a large amount of computer memory but also a longer calculation time.

Potyondy and Cundall (2004) demonstrated scale effect is not significant in rock modelling under compressive loading conditions. Initial modelling was conducted at various scales to evaluate model run times and model size. Our findings were consistent with those of Potyondy and Cundall (2004) and indicated that provided the particle diameter is relatively small compared to the model size, modelling full scale is not required. A 25%-scaled model (i.e., sample dimension, loading position, moment arm) provided an optimum model size with reasonable run times while not compromising the output. The scaled model dimension was 100 mm × 22 mm but out of the plane dimension was set to unit thickness since PFC2D model represents the assembly of circular disks with unit thickness. A total of 7,000 disks were generated for the model.

The axial loading platen was modelled as single clumped particle so that the plate itself moved as a rigid body transferring the boundary load to the specimen. This system produces a uniform axial stress in the beam. The plate thickness was chosen as 5% of the beam length similar to the thickness applied in the laboratory test. The interface layer between the specimen and the platen was created with particles with a diameter of 0.5 mm. Bearing

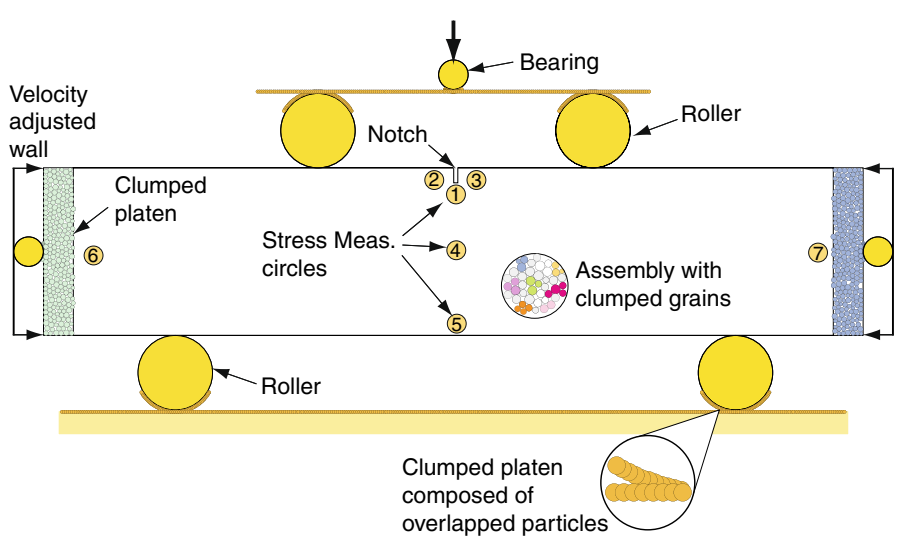


**Fig. 12** Illustration shows the model setup used to simulate the axially compressed bending test in PFC2D. Also shown are the locations of the measurement *circles*

balls were installed on the clumped plate to mimic the laboratory test system with the friction on any contact points on these balls set to zero. These bearing balls act as a hinge to minimize the potential to create a moment or eccentricity, and also transfer the external loads to the specimen.

Four specific balls were used to mimic the rollers with the two bottom balls sitting in semi-circular platen composed of overlapped clump particles. Both the contact friction and shear stiffness of these balls were set to zero such that the balls were free to roll and rotate. The hydraulic rams were modelled by installing velocity walls on the top bearing and side bearing balls. The notch was installed at the top of beam centre by eliminating balls whose centre position was within the notch geometry.

Application of vertical loading to the beam was activated by applying a vertical force on the bearing ball located at the top platen. Horizontal axial loads were activated by applying a specific velocity to the walls that corresponds to the force calculated from the vertical force applied to top bearing ball. The wall velocity was adjusted every iteration to maintain the specified loading ratio for bending and axial loading. This wall velocity control was developed using the wall servo control logic in "FISH-TANK" of PFC (Itasca Consulting Group 2004).

The stress in PFC was obtained using a measurement circle. The particle stresses whose centroid is within the circle are calculated by summating the contact forces for particle volume and then, summation of particle stresses within the region are averaged by the measurement circle volume. Using this measurement circle, principal stresses and their orientation could be traced during the simulation. A total of seven measurement circles were installed in the beam (Fig. 12). Three measurement circles were installed right below and beside the notch. Others were positioned at the centre, and bottom fibre of the beam, and just beside the axial loading platen to trace the stress path during loading.

Both axial and vertical loads were applied simultaneously in 1 kPa increments per 100 cycles or when the average unbalanced force in the system was below a certain tolerance. The load increment involves a loading rate thus each load increment must be low enough to maintain a stable loading system. The loading interval was chosen based on the findings given in Cho et al. (2007) and was sufficiently small to ensure the system was in equilibrium before the application of the next loading increment. This logic was also developed using FISH (Itasca Consulting Group 2004).

Axial and vertical loads were applied to the particle assembly until the sample ultimately ruptured and Fig. 13 shows the load ratio measured during this process. Figure 13 shows that a load ratio of approximately 3 was maintained until the specimen ultimately ruptured.

## 5 Results

Figure 14 compares the stress measured at the notch tip in PFC with the calculated results using the laboratory test and Eq. 3.1. Both PFC and the laboratory results are in reasonable agreement in Fig. 14 up to approximately 15 MPa with the results showing increasing divergence above approximately 12 MPa. Recall that the laboratory stresses were elastic stresses and that the onset of non-linear behaviour and dilation in the laboratory results occurred at approximately 12 MPa. This agrees reasonably well with the peak strength of approximately 15 MPa given by PFC. The slight strain hardening that occurs above 15 MPa in PFC is likely related to the difficulty of maintaining a completely stable system once the sample started to fail. This rapid onset of failure once spalling initiated was also observed in the laboratory tests.

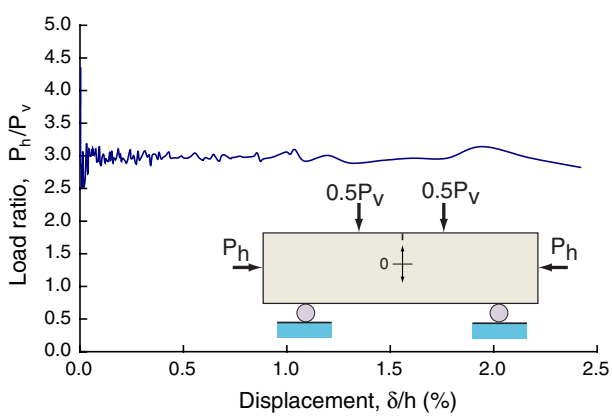


**Fig. 13** Load ratio measured during the PFC simulation. The displacement $\delta$ was measured at the *bottom midpoint* of the beam

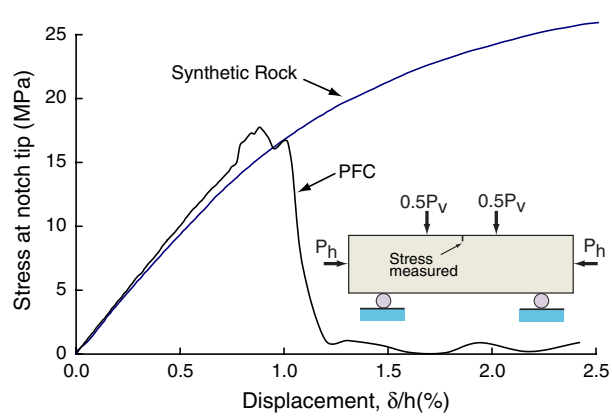


**Fig. 14** Comparison of notch tip stress in PFC and the calculated stress determined using the laboratory test results and Eq. 3.1

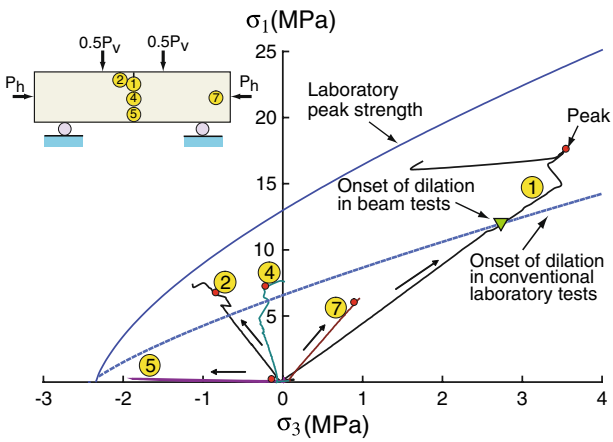


**Fig. 15** Illustration of the stress paths followed at several locations as the sample is loaded and fails. The *small red circles* on each stress path show when the stress below the notch reaches its peak value

Figure 15 shows the stress path obtained from within the measurement circles during the numerical simulation. The laboratory peak strength envelope and the onset of the dilation boundary, defined as the onset of extensile axially aligned cracking, in Fig. 15 for the synthetic rock was given in Cho et al. (2007). The measured stress path in Fig. 15 illustrates that the centre of the specimen experiences several different stress path that depends on the location of the measurement. Stress path 1 and 2 in Fig. 15 are the stresses measured near the notch tip but they have quite different stress paths. Path 1 follows non-monotonically increasing compressive stress path while path 2 displays tensile loading similar to a Brazilian test stress path. Stress path 7 is similar to the non-monotonic stress path shown in path 1. This may be related to the confining effect of the end platen combined with non-uniformly distributed boundary stresses. Stress path 4 is similar to the stress path 2. Path 5 shows the typical stress path observed in direct tension test but it is only observed after the notch stress reach its peak value in stress path 1.

In Fig. 15, the red circles in each stress path show the stress level when the stress below the notch reaches its maximum value in stress path 1. Interestingly, none of stress paths shown in Fig. 15 reach the peak strength envelope obtained from the traditional laboratory test, i.e., Brazilian, uniaxial and triaxial compression. However, stress paths 1, 2 and 4 which measure the stress in the vicinity of the notch all exceed the onset of dilation, i.e., the onset of extension cracking measured in the laboratory tests. Note that from Figs. 8, 9 and 14, the onset of dilation and visible cracking at the notch tip occurred when the stress magnitude at the notch tip reached approximately 12 MPa. In Fig. 15 this value of 12 MPa agrees with the intersection of the onset of laboratory dilation. This is similar to the results reported by Martin et al. (1997) and

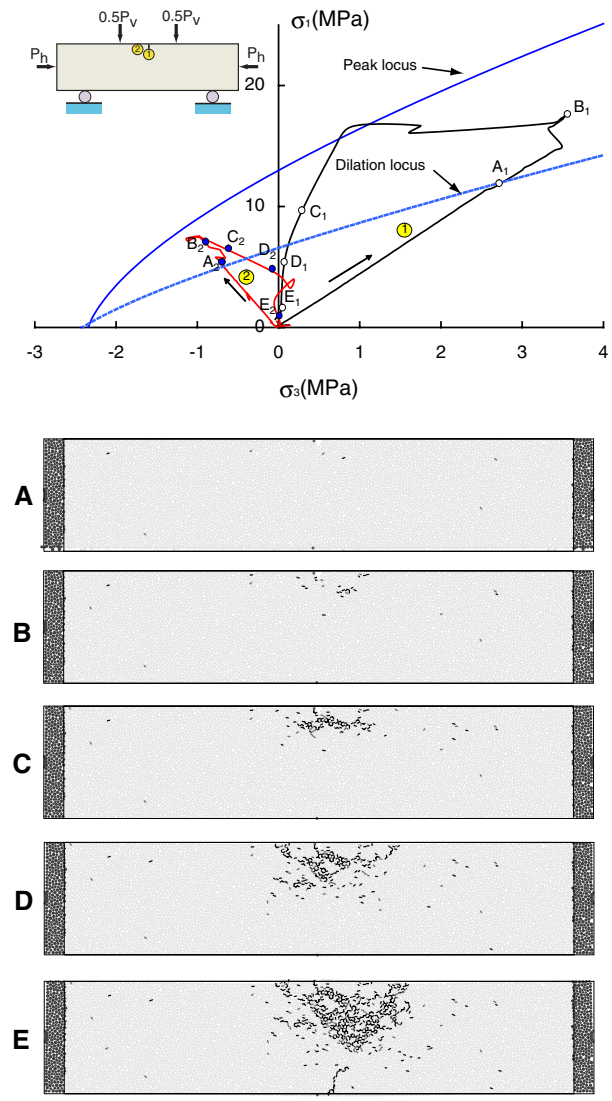


**Fig. 16** Stress path near the notch and fracture development by stage. The peak strength envelope is based on traditional laboratory tests, i.e., Brazilian tensile tests, and uniaxial and triaxial compression tests. Note that the onset of dilation in the bending tests occurred at approximately 12 MPa

Andersson (2007) that the stress magnitudes required to cause visible spalling in situ is similar to the stress magnitudes required to cause crack-initiation in laboratory tests.

Figure 16 shows the stress path evolution near the notch tip (i.e., path 1 and path 2) with the fracture development within the specimen. The subscript for each stage denotes the stress path number. As stress path 1 reaches the dilation locus (stage A in Fig. 16) cracks initiates near the notch and the specimen begins to experience a localised complex stress path because of the redistribution of stress associated with the crack formations. Interestingly, at this stage in stress path 2, the stresses also reach the dilation locus in the tensile region. The subsequent stress changes above the

dilation locus induce more cracks and these new cracks reduce the actual confinement (stage B in Fig. 16). This crack-induced process continues until the volume in the centre of the beam is essentially destressed.

The fractures in the PFC simulation become more localised after the peak stress is reached. The stress-induced fracture pattern naturally evolves into a v-shaped notch that is essentially destressed (stage D in Fig. 16). This depth of notch development is a function of the loading and boundary conditions. In our samples as notch development occurs the moment of inertia of beam is reduced and tensile rupture at the bottom occurs (stage E in Fig. 16). Note that in Fig. 16 the v-shaped notch is not centred in the middle of the beam, despite the loads being applied equally at both ends of the beam. In all the numerical models examined, the exact position and shape of the v-shaped notch varied slightly with each run, reflecting the non-uniqueness of the discrete element solution.

Figure 17 compares the notch stress and the number of cracks produced by shear and tension in the PFC sample at each stage. The fractures occurring in the discrete element specimen by either tension or shear are identified by measuring the forces mobilized in the bonds between the particles. If the mobilized shear forces in the bonds exceeds the specified micro shear bond strength, then bond breakage is counted as a shear crack while if the mobilized tensile forces in the bond exceeds the specified micro normal bond strength then bond breakage is counted as tension cracks. Using this approach it was possible to evaluate the number of shear or tensile cracks at each stage of the test.

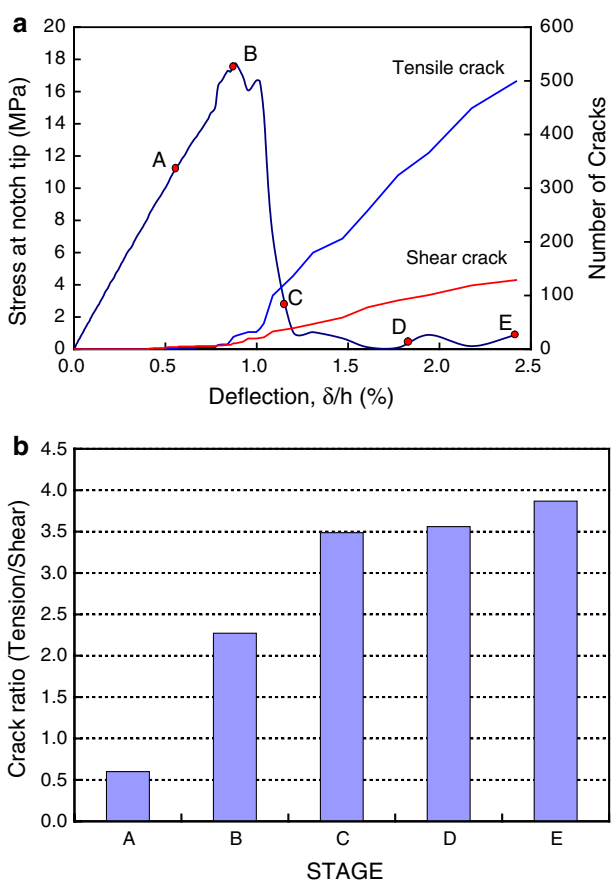


**Fig. 17** Number of cracks generated by stage. **a** Number of cracks, **b** crack ratio

In Fig. 17a, before the peak notch stress, the number of shear and tension cracks is similar. However, after the peak stress is reached and as the notch develops the number of tension cracks relative to the number of shear cracks increases significantly (see Fig. 17b). This is likely attributed to the reduction in confinement that occurs as the notch develops. It should be noted that the majority of the bonds that break in tension are located in the upper half of the beam where the overall loading is compressive.

## 6 Discussion and Conclusions

In both uniaxial and triaxial conventional laboratory compression tests researchers (e.g., Brace et al. 1966; Lajtai 1974; Martin and Chandler 1994) using cylindrical specimens have shown that the onset of dilation is associated with lateral expansion of the specimen due to the opening of axially aligned cracks. Diederichs (2003) suggested that should this crack-induced dilation initiate near the boundary of a cylindrical specimen, these axially aligned open cracks would increase the confinement on the interior of the sample suppressing the extension of additional cracks in the centre of the sample. Hoek (1968) demonstrated that open inclined cracks in compression can only propagate if the stresses near the crack tip remain tensile and Horii and Nemat-Nasser (1985) showed that the crack-opening force required to create this tension was very sensitive to compressive boundary conditions. Hence, for a single open crack to grow longer the zone of tensile stress must encompass a large region and in small laboratory cylindrical samples this is difficult to achieve. Hence it appears that the size of the samples and the cylindrical boundary condition are probable reasons for spalling not being observed in laboratory compression tests at a stress level associated with the onset of dilation.

In our axially compressed bending test the non-uniformly distributed stresses result in the maximum tangential stresses near the top of the beam. Once cracking begins at the notch tip spalling progressively propagates downwards towards the region of lower tangential stress. In the final stages of rupture the progressive nature of the spalling process causes the bottom portion of the beam to failure in tension.

The measurements of beam displacement showed that the onset of dilation in our beams occurred when the calculated maximum stress beneath the notch tip reached approximately 12 MPa. Numerical analysis using the DEM also showed that near the notch tip dilation occurred when the $\sigma_1$ stress reached approximately 12 MPa. Spalling in our beam tests based on displacement and the onset on non-linear response began at approximately the same stress level. The onset of dilation based on this numerical modelling shows that it occurs well below the peak strength envelope determined from conventional laboratory tests and hence spalling in our beam tests also occurred before the laboratory peak strength was reached.

Andersson (2007) and Martin (1997) showed that in crystalline rock spalling occurred when tangential stresses on the boundary of circular excavations reached approximately 50% of the laboratory uniaxial compressive strength and this stress level agreed with the onset of dilation measured in conventional laboratory tests. It would appear based on their results and the results from our bending tests that the onset of dilation is a more reliable indicator for predicting the stress levels associated with spalling.

Our test results suggest that this test configuration is suitable for exploring the spalling process. However, it is also clear from these tests that our results would have benefited from servo-controlled loading system. Once spalling initiated, rupture of the beams quickly followed regardless of our loading rate. The application of these test configurations to beams of granite would also require a redesign of the load system to ensure it had compatible stiffness with the sample stiffness.

**Acknowledgments** This work was supported by the Natural Sciences and Engineering Research Council of Canada, the Swedish Nuclear Fuel and Waste Management Co.

## References

Andersson JC (2007) Äspö Pillar stability experiment: rock mass response to coupled mechanical thermal loading. PhD thesis, Royal Institute of Technology (Kungliga Tekniska Högskolan), KTH, Stockholm

Brace WF, Paulding B, Scholz C (1966) Dilatancy in the fracture of crystalline rocks. J Geophys Res 71:3939–3953

Cho N, Martin CD, Sego DC (2007) A clumped particle model for rock. Int J Rock Mech Min Sci 44:997–1010

Diederichs MS (2003) Rock fracture and collapse under low confinement conditions. Rock Mech Rock Eng 36(5):339–381

Dzik EJ (1996) Numerical modeling of progressive fracture in the compression loading of cylindrical cavities. PhD, University of Manitoba

Ewy RT, Cook NGW (1990) Deformation and fracture around cylindrical openings in rock—I. Observations and analysis of deformations. Int J Rock Mech Min Sci Abstr 27:387–407

Fairhurst C, Cook NGW (1966) The phenomenon of rock splitting parallel to the direction of maximum compression in the neighbourhood of a surface. In: Proceedings of the 1st congress of ISRM, pp 687–692

Gay NC (1973) Fracture growth around openings in thickwalled cylinders of rock subjected to hydrostatic compression. Int J Rock Mech Min Sci Abstr 10:209–233

Haimson BC, Song I (1993) Laboratory study of borehole breakouts in Cordova cream: a case of shear failure mechanism. Int J Rock Mech Min Sci Abstr 30:1047–1056

Hibbeler RC (1997) Mechanics of material. Prentice-Hall, Englewood Cliffs

Hoek E (1965) Rock fracture under static stress conditions. National Mechanical Engineering Research Institute, Council for Scientific and Industrial Research, MEG383

Hoek E (1968) Brittle failure of rock. In: Stagg KG, Zienkiewicz OC (eds) Rock mechanics in engineering practice. Wiley, New York, pp 99–124

Horii H, Nemat-Nasser S (1985) compression-induced microcrack growth in brittle solids: axial splitting and shear fracture. J Geophys Res 90:3105–3125

Itasca Consulting Group (2004) PFC2D (particle flow code in 2 dimensions) version 3.1

Lajtai EZ (1974) Brittle fracture in compression. Int J Fract Mech 10:525–536

Lee M, Haimson B (1993) Laboratory study of borehole breakouts in Lac Du Bonnet granite: a case extensile failure mechanism. Int J Rock Mech Min Sci Abstr 30:1039–1045

Lipson C, Juvinall RC (1963) Handbook of stress and strength. Macmillan, New York

Martin CD (1997) Seventeenth Canadian geotechnical colloquium: the effect of cohesion loss and stress path on brittle rock strength. Can Geotech J 34:698–725

Martin CD, Chandler NA (1994) The progressive fracture of Lac du Bonnet granite. Int J Rock Mech Min Sci Abstr 31(6):643–659

Martin CD, Martino JB, Dzik EJ (1994) Comparison of borehole breakouts from laboratory and field tests. In: Proceedings of the EUROCK'94, SPE/ISRM rock mechanics in petroleum engineering, Delft, A.A. Balkema, Rotterdam, pp 183–190

Martin CD, Martino JB, Read RS (1997) Observations of brittle failure around a circular test tunnel. Int J Rock Mech Min Sci 34:1065–1073

Martin CD, Kaiser PK, McCreath DR (1999) Hoek-Brown parameters for predicting the depth of brittle failure around tunnels. Can Geotech J 36:136–151

Potyondy DO, Cundall PA (2004) A bonded-particle model for rock. Int J Rock Mech Min Sci 41:1329–1364

RocScience Inc. (2002a) Phase2D. http://www.rocscience.com

RocScience Inc. (2002b) RocLab 1.007. http://www.rocscience.com

Santarelli FJ, Brown ET (1989) Failure of three sedimentary rocks in triaxial and hollow cylinder compression tests. Int J Rock Mech Min Sci 26:401–413

Sellers EJ, Klerck P (2000) Modelling of the effect of discontinuities on the extent of the fracture zone surrounding deep tunnels. Tunelling Undergr Space Technol 15:463–469

Tapponnier P, Brace WF (1976) Development of stress-induced microcracks in westerly granite. Int J Rock Mech Min Sci Abstr 13:103–112